# Role of the Exposed Polar Facets in the Performance of Thermally and UV Activated ZnO Nanostructured Gas Sensors

Mohammad R. Alenezi, Abdullah S. Alshammari, K. D. G. I. Jayawardena, Michail J Beliatis, Simon J. Henley, and S. R. P. Silva*

Nanoelectronics Center, Advanced Technology Institute, University of Surrey, Guildford, GU2 7XH, United Kingdom

ABSTRACT: ZnO nanostructures with different morphologies (nanowires, nanodisks, and nanostars) were synthesized hydrothermally. Gas sensing properties of the as-grown nanostructures were investigated under thermal and UV activation. The performance of the ZnO nanodisk gas sensor was found to be superior to that of other nanostructures ($S_g \sim$ 3700% to 300 ppm ethanol and response time and recovery time of 8 and 13 s). The enhancement in sensitivity is attributed to the surface polarities of the different structures on the nanoscale. Furthermore, the selectivity of the gas sensors can be achieved by controlling the UV intensity used to activate these sensors. The highest sensitivity value for ethanol, isopropanol, acetone, and toluene are recorded at the optimal UV intensity of 1.6, 2.4, 3.2, and 4 mW/cm^2, respectively. Finally, the UV activation mechanism for metal oxide gas sensors is compared with the thermal activation process. The UV activation of analytes based on solution processed ZnO structures pave the way for better quality gas sensors.
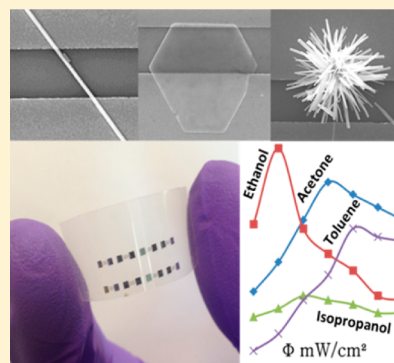
1. INTRODUCTION

The controlled synthesis of nanostructures has progressed rapidly in the past decade. Understanding the relationship between morphology, property, and application is very important to fabricate highly functional materials for practical devices. Gas sensors are of significant interest among these devices because of their essential role in a number of important fields, including industrial process control, safety systems, disease diagnoses, and environmental monitoring.[1−8]

Metal oxide nanostructures have numerous advantages as gas sensors such as high sensitivity, short response time, and self-refreshability. Due to their small dimensions, the electrical resistance of the nanostructures is susceptible to changes at their surface, as the length scales of surface interactions are comparable to the dimensions of the nanomaterial.[1−8] The sensing mechanism of metal oxide nanostructures is based on the activation of atmospheric oxygen on the surface at high temperatures. Consequently, the catalytic reactions of gaseous species with oxygen sites on the surface induce charge transfer from the surface to the bulk, which changes the electrical resistance of the device. Therefore, the chemical adsorption and reaction of target molecules occurring on the surface of metal oxide semiconductors is the most crucial factor controlling the gas sensing behavior.[6−8]

In previous years, the influence of the morphology, size, and surface area of metal oxide nanostructures on their gas sensing properties has been investigated extensively.[9−12] For example, Xie et al.[12] investigated the effect of the exposed facets on the gas sensing properties of ZnO thin film in comparison to those of a ZnO NW array. The authors attributed the enhancement in the performance of the ZnO NW array gas sensor, high sensitivity (3-fold prefactor Ag), fast response (less than 10 s),

and low detection limit (1 ppm) to benzene and ethanol, to the exposed polar facets. However, their study did not consider the differences in dimensionality as well as the surface-to-volume ratio between the thin film and NW array gas sensors. Additionally, in the NW array structure, most of the exposed facets are nonpolar facets similar to the thin film exposed facets. Therefore, it is not accurate to attribute the enhanced performance of the NW array gas sensor to the exposed polar facets only. Until now, probably due to poor morphology-controlled syntheses of metal oxide nanostructures, systematic studies concerning the relation between the crystal planes of metal oxide and gas sensing properties are not well reported.[12] Hence, it is challenging to attribute and correlate the effect of the exposed crystal surfaces of metal oxide nanomaterials to their gas sensing properties.

Despite the various attractive features of metal oxides as gas sensors, it is technically difficult to detect chemicals with thermally activated gas sensors. The high energy consumption and large size of the sensors prove difficult to incorporate additional heating elements, temperature controllers, and signal processing elements on a single electronic platform. Besides, operating the device at high temperature reduces its durability. Therefore, an alternative to the thermal activation mechanism is preferable. A number of successful attempts were reported through photoactivation of metal oxide films by exposure to ultraviolet (UV) radiation,[13−16] which allow the possibility of gas sensing at room temperature. The implementation of these UV activated metal oxide gas sensors in different fields for

portable and flexible devices or low power consumption applications then becomes possible.

In this paper we address three key aspects of gas sensors; i.e., the 3S's (Sensitivity, Stability, and Selectivity). We start by reporting the morphology controlled syntheses of different ZnO nanostructures along with the corresponding gas sensing properties. Typical ZnO nanostructures such as nanowires (ZNWs), nanodisks (ZNDs), and nanostars (ZNSs), with different ratios of exposed polar to nonpolar facets, are successfully synthesized via facile hydrothermal method using different growth solutions. Electron microscopic studies are applied to characterize the morphology and surface structures of the as-prepared ZnO nanostructures. The gas sensing properties of the ZnO nanostructures under thermal and UV activation are investigated. Additionally, we demonstrate how controlling the intensity of the UV irradiation can be used to tune the selectivity of the ZND sensors to target volatiles. Furthermore, in an effort towards lowering the operating temperature to enhance the stability of gas sensors, we compare the thermal and UV activation mechanisms for ZnO gas sensors. A model of the room temperature UV activated sensor is discussed based on our results. Finally, the gas sensing responses of the different ZnO nanostructures are explained based on the structural analysis of various crystal planes (i.e., surface polarities).

2. EXPERIMENTAL DETAILS

2.1. Preparation of ZnO Nanostructures. All reagents in this work were analytical grade. The growth of ZNWs starts by preparing a seeded substrate. Silicon (Si) substrates were cleaned by sonication in acetone, isopropyl alcohol (IPA), ethanol, and deionized water for 10 min each, consecutively. Further, it was dried with nitrogen gas and baked on a hot plate at 150 °C for 5 min. The substrate was then spin coated with 5 mM zinc acetate dehydrate $Zn(CH_3COO)_2 \cdot 2H_2O$ solution in ethanol at 1000 rpm for 30 s. The spin-cast layer on the silicon substrate was cured on a hot plate 150 °C for 5 min to stabilize the film structure. The spin coating and curing processes were repeated five times in order to obtain a uniform film, which served as the seeding layer. Afterward, the film was thermally annealed at 350 °C for 30 min, and then allowed to cool down. The thermal decomposition (of the zinc acetate) created ZnO nanocrystals on the substrate that act as a seed layer for subsequent ZnO array growth. The precursor solution for the hydrothermal reaction consists of 25−50 mmol zinc nitrate, 12.5−25 mmol HMTA, and 350−450 mmol ammonium hydroxide. The seeded substrate was then placed in a vial that contains (15 mL) of the growth solution. 5 mmol polyethylenimine (PEI) (end-capped, molecular weight 800 g/mol LS, Aldrich) was also added to the growth solution as a capping agent to control the diameter of the nanowires. The vial was covered and then placed in an oven which had been preheated to 90 °C to start the growth of ZnO arrays. It takes several minutes for the growth solution to reach 90 °C. The vial was taken out of the oven after 24 h, and the silicon substrate was transferred to a new vial containing only warm DI water for another 24 h to dissolve PEI residuals. The substrate was then rinsed with DI water and dried in air at 150 °C for 30 min. Finally, the ZnO array was sonicated in ethanol for few minutes to remove the nanowires from the substrate.

ZNSs are grown using the same growth temperature, time, and solution used to grow the ZNWs but without using a seed

layer. When the growth is performed, the grown ZNSs are filtered and kept in ethanol.

In the typical growth process for ZNDs, a mixture of (100 mmol) zinc sulfate $(ZnSO_4)$ and (100 mmol) hexamethylenetetramine (HMTA) is stirred at room temperature to make a homogeneous solution. The mixture is transferred to a vial and heated to 75 °C in an oven for 3 h. After that, the grown nanostructures are filtered and transferred to another vial containing ethanol.

2.2. Structure and Morphology Characterization. The crystal structure of the as-prepared products were analyzed through powder X-ray diffraction (XRD) using a Panalytical X-pert diffractometer with Cu Kα radiation. The morphology and crystal structure of as-prepared products were observed using Philips XL-20 scanning electron microscope at 10 kV. Scanning transmission electron microscopy (STEM) and electron diffraction measurements were performed on a Hitachi HD2300A microscope operating at 200 kV. STEM samples were prepared by depositing a drop of diluted suspension of the nanostructure in ethanol on a carbon film coated copper grid. The surface composition of the ZnO samples were determined using PHI QUANTUM 2000 photoelectron spectrometer (XPS) using a monochromatic magnesium X-ray source. The binding energies were calibrated with respect to the signal for adventitious carbon (binding energy of 284.6 eV). Photoluminescence (PL) spectroscopy was performed at room temperature using a Cary Eclipse spectrometer with an excitation wavelength of 325 nm.

2.3. Device Fabrication and Testing. ZNW, ZND, and ZNS gas sensors were fabricated by spin coating solutions containing these nanostructures, respectively, on SiO_2/Si and plastic substrates with prepatterned gold electrodes. The spacing between the electrodes was 5 μm. Before measurement, sensors fabricated using SiO_2/Si substrates were further aged at 300 °C for 2 days to improve the stability before testing. Devices on SiO_2/Si substrates were tested as thermally and UV activated gas sensors for comparison, while those with plastic substrates were only tested as UV activated sensors. The gas sensing properties were measured using a homemade gas sensing chamber attached to a Keithley 4200 semiconductor analyzer. The excitation source for the UV light was a UV lamp with maximum intensity at a wavelength of 365 nm. The intensity of the UV was controlled by changing the distance between the source and the sensor.

The sensor response, S_g, is defined as $S_g = (I_g - I_a)/I_a$, where I_g is the sensor current value in the tested gas environment and I_a is the current value in air. The measurements were done under fixed bias. The response time, t_r, is defined as the time required for the current to reach 90% of the equilibrium value after injecting the gas, and the recovery time, t_d, is defined as the time necessary for the sensor to return to 10% above the original current value in air after releasing the gas from the test chamber.

3. RESULTS AND DISCUSSION

3.1. Morphology and Structure. ZnO is a wurtzite-structured crystal and usually described as a number of alternating planes composed of tetrahedrally coordinated O^{2-} and Zn^{2+} ions stacked alternatively along the c-axis.[17] Such a structure type causes a divergence in the surface energy of polar (0001) surface, and a strong anisotropy in the growth rate ν, such as $\nu \, [0001] \gg \nu \, [10\overline{1}0]$. Therefore, wurtzite-type ZnO nanostructures usually tend to minimize the exposed areas of

the {0001} polar facets which possess high surface energy, and maximize the exposed areas of the {10$\bar{1}$0} nonpolar facets. So, by controlling the growth environments of ZnO nanostructures, the morphology and exposed surfaces can be tuned.[18]

Figure 1a shows a typical SEM image of a ZNW gas sensor with an 8 μm long and 200 nm diameter ZNW between the
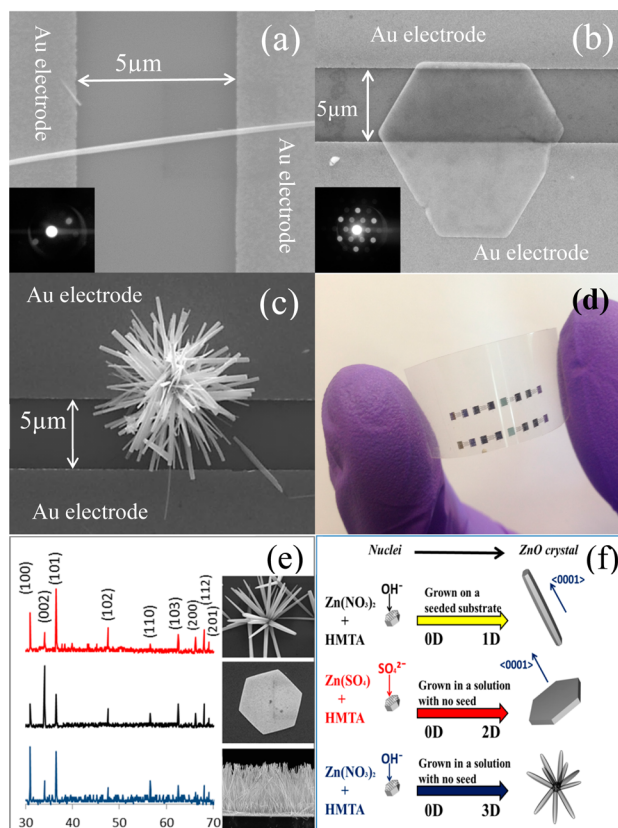
Figure 1. (a) SEM image of a ZNW gas sensor (inset: SAED pattern of ZNWs), (b) SEM image of ZND gas sensor (inset: SAED pattern of ZNDs), (c) SEM image of ZNS gas sensor, ZnO nanostructured sensors on flexible substrate, (e) XRD patterns and the corresponding SEM images of ZNWs, ZNDs, and ZNSs, and (f) schematic diagram of the growth process of ZNWs, ZNDs, and ZNSs.

electrodes. ZNWs are single crystals growing along the [0001] direction as confirmed by the selected area electron diffraction (SAED) pattern in the inset of Figure 1a and their side surfaces are nonpolar {10$\bar{1}$0} planes, as is typically reported in the literature.[1−5] An SEM image of a ZND gas sensor, where a very thin ZND bridges the two gold electrodes, is shown in Figure 1b. The SAED pattern of the ZNDs, shown in the inset of Figure 1b, confirms that they are single crystals. The thickness of the ZNDs is uniform in the range of tens of nanometers as evident from the transparent nature under the electron beam in the SEM. Figure 1c shows an SEM image of a ZNS gas sensor where a ZNS consists of many nanowires with diameters in the range of 150−200 nm bridging the sensor electrodes. Multiple devices on a flexible plastic substrate are shown in Figure 1d.

The XRD patterns of the three grown nanostructures are shown in Figure 1e with an SEM image of each nanostructure in the inset next to its XRD pattern. It is found that all as-prepared structures are highly crystalline, and the diffraction peaks in every pattern can be indexed as belonging to hexagonal wurtzite-type ZnO (JCPDS No. 36−1451). No peaks due to

impurities were detected, indicating that all zinc salt precursors have been thoroughly decomposed into pure ZnO during the reaction and any excess removed during cleaning. However, the diffraction intensity ratios of (0002) polar plane to (10$\bar{1}$0) nonpolar plane ($I_{(0002)}/I_{(10\bar{1}0)}$) for ZNWs, ZNDs, and ZNSs are 0.36, 2.1, and 0.5, respectively.

The low intensity ratio of the hydrothermally grown NWs in this work is unlike the usual observation of high intensity ZnO (002) peak in XRD analysis of ZnO NW arrays in the literature. The high intensity ZnO (002) peak represents the good alignment of the NWs growing in the c direction. The NWs in this work showed a lower intensity (002) peak because they are relatively long with low density leading to poor alignment (NW array SEM image in the inset of Figure 1e). Additionally, these NWs can easily break and lie on the substrate. On the other hand, the high diffraction intensity ratio for the ZNDs indicates that there are more structures with their c direction normal to the substrate than for the ZNWs and ZNSs.[19]

The above structural characterization results demonstrate that the ZnO nanostructures prepared via different synthetic routes have different exposed ratios of polar surfaces. The ZNWs and ZNSs are dominated by their nonpolar {10$\bar{1}$0} planes, while the dominant surfaces for ZNDs are the (0001) polar planes. These grown nanostructures provide an opportunity to systematically investigate the interaction between exposed planes of ZnO nanocrystals and related physicochemical properties.

In the hydrothermal process, ZnO tends to form one-dimensional structures, since the crystal growth is faster along [0001] than along other directions.[18] Therefore, in the growth process of ZNWs, ZnO nanoparticles in a seed layer only grow upward because all other directions are blocked by the neighboring nanoparticles. However, ZnO nanoparticles in a solution grow in every possible direction like a star because they have access to the growth solution from every direction, which results in the formation of ZNSs as shown in the schematic diagram in Figure 1f.

Recently, it was reported that changing the counterion for zinc often results in the production of different crystallite morphologies.[20] Morphological changes originate mainly from the effects of the promoter species that obstructs nucleation and disrupts the growth processes in selected crystallographic directions. In the present case, the shape of the hexagonal ZNDs is attributed to anisotropic growth, where the lateral growth rate is much greater than the growth rate in the c-axis direction. The (0001) and (000$\bar{1}$) facets of ZnO crystal have equal reticular density, but they are different in composition of the outermost atomic layer. The effective charge is positive on the outermost layer of the (0001) facet, consisting of Zn^{2+} ions, while the outermost layer of the (000$\bar{1}$) facet, consisting of O^{2-} ions, has a negative charge of the same magnitude. As a result, the counterions (SO_4^{2-}) from the raw material are adsorbed on the (0001) surface rather than (000$\bar{1}$), which hinders the attachment of growth units of $[Zn(OH)_4]^{2-}$ onto the (0001) surface. Consequently, the intrinsically anisotropic growth of ZnO along the [0001] direction is substantially suppressed and crystal growth, then proceeds sideways forming hexagonal ZNDs as shown in the schematic diagram in Figure 1f.

3.2. Gas Sensing Properties of ZNWs, ZNDs, and ZNSs. ZNW, ZND, and ZNS gas sensors did not show any sensitivity to volatiles, such as ethanol, when operated at room temperature in the dark. This is in agreement with the work reported by Saura et al.[15] and theoretical investigations on the

mechanism of UV illumination[16] which states that the metal oxide sensors are not sensitive without UV illumination due to the thermally stable nature of chemisorbed oxygen at room temperature. However, the sensors responded well when the operating temperature was increased and when tested under UV illumination at room temperature as shown in Figure 2.
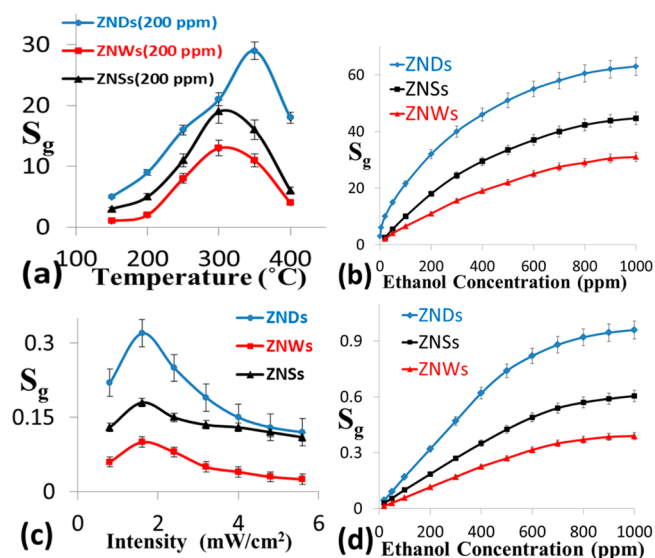
Figure 2. (a) Responses of ZNW, ZND, and ZNS sensors to 200 ppm of ethanol at different temperatures. (b) Response vs time curves of ZNW, ZND, and ZNS sensors to different ethanol concentrations at 350 °C. (c) Responses of ZNW, ZND, and ZNS sensors to 200 ppm of ethanol at different light intensities. (d) Response vs time curves of ZNW, ZND, and ZNS sensors to different ethanol concentrations at 1.6 mW/cm².

In order to investigate the effect of changing the morphology of the nanostructures and the corresponding variation in the ratio of polar to nonpolar exposed facets on their performance as gas sensors, all fabricated sensors were tested under thermal and UV activation. Thermally activated gas sensors were tested at different temperatures to find out the optimum operating condition for ethanol detection. Figure 2a shows the responses of the ZNW, ZND, and ZNS sensors (defined as $S_g = (I_g - I_a)/I_a$, where I_g is the sensor current value in the tested gas environment and I_a is the current value in air) to 200 ppm ethanol at different operating temperatures. The responses of sensors are found to increase with increasing operating temperature, with a maximum response for ZNW, ZND, and ZNS sensors being observed at 300, 350, and 300 °C, respectively, and then decrease with a further rise of operating temperature. This behavior of the sensitivity as a function of the operating temperature is usually explained with regard to the kinetics and mechanics of gas adsorption and desorption on the surface of ZnO or similar semiconducting metal oxides.[21] When the operating temperature is too low, the chemical activation of the sensor is consequently small, leading to a small response. When the operating temperature is increased beyond a threshold value, some adsorbed gas molecules may escape before the charge transfer due to their enhanced activation, thus the response will decrease correspondingly. However, this justification does not explain why different ZnO nanostructures have different optimum operating temperatures for the same tested gas, which we will discuss later in this paper.

Furthermore, analyzing the sensitivity of the different morphologies indicates that at this level of ethanol concentration (200 ppm) the sensitivity of the ZND sensor is much higher than those of ZNWs and ZNSs over the entire temperature range. The sensitivity of ZND sensor reaches 29 at the optimal working temperature of 350 °C, while the sensitivities of ZNW and ZNS sensors are 11 and 17, respectively.

Response versus ethanol concentration curves of three thermally activated gas sensors at 350 °C are shown in Figure 2b. For ethanol at levels of 100, 300, and 500 ppm, the ZND sensor responses are 20, 37, and 48, respectively. The ZNW responses to the same ethanol levels are 6.5, 14.5, and 20.5, respectively, while the responses of the ZNS sensor to the same ethanol levels are 11, 22.5, and 32.5, respectively. Furthermore, we note that ZNW and ZNS sensors do not show any sensitivity to ethanol at levels below 20 ppm.

UV activated gas sensors were also tested at different UV light intensities at room temperature. Figure 2c shows the responses of all sensors to 200 ppm ethanol at different UV light intensities. In all cases the performance of the ZND sensor is found to be superior to those of ZNW and ZNS sensors. The sensitivity of ZND sensor reaches 0.32 at the optimal working intensity of 1.6 mW/cm², while the sensitivity values of ZNWs and ZNSs are 0.1 and 0.18 at the same intensity. Interestingly, the maximum sensitivity was not achieved by using the UV source at maximum intensity. Generally these observations are not in agreement with the mechanistic study[19] which stated that theoretically, the sensitivity should increase with increasing UV radiation flux density. The decay in sensitivity of the UV activated gas sensors above a UV intensity threshold value will be discussed in more detail later in this paper.

The responses of the UV activated gas sensors to different ethanol concentrations at the optimum intensity are shown in Figure 2d. For the ZND sensor, the response values for ethanol at levels of 100, 300, and 500 ppm are 0.17, 0.47, and 0.73, respectively, while the ZNS sensor responses for the same ethanol levels are 0.1, 0.25, and 0.41, respectively. The ZNW sensor response, which is the lowest, for the same ethanol levels is 0.05, 0.16, and 0.27, respectively.

The sensor response (S_g) relation to ethanol concentration (C_g) can be empirically represented by[22]

$$S_g = aC_g{}^{\beta} + 1 \tag{1}$$

where a is a parameter and β is the surface species charge parameter having value of 1 for O^- and 0.5 for O^{2-}. Equation 1 can be rewritten as

$$\log(S_g - 1) = \log a + \beta \log C_g \tag{2}$$

Figure 3a,b shows plots of $\log(S_g - 1)$ versus $\log C_g$ for the thermally and UV activated ZND sensors, respectively, where a linear relationship as described by eq 2 is observed. The values of β of the thermally and UV-activated sensors were 0.577 and 1.042, respectively. This suggests that the dominant adsorbed oxygen species at the surface of the thermally activated ZND sensor are O^{2-} ions, while the adsorbed oxygen species at the surface of the UV-activated ZND sensor are O^- ions.[22]

At ethanol concentration levels above 1000 ppm, the sensitivity of the thermally and UV activated sensors show evidence of saturation. This can be explained by a competition between the adsorption sites versus the concentration of target gas. At low gas concentration levels, there are infinite available
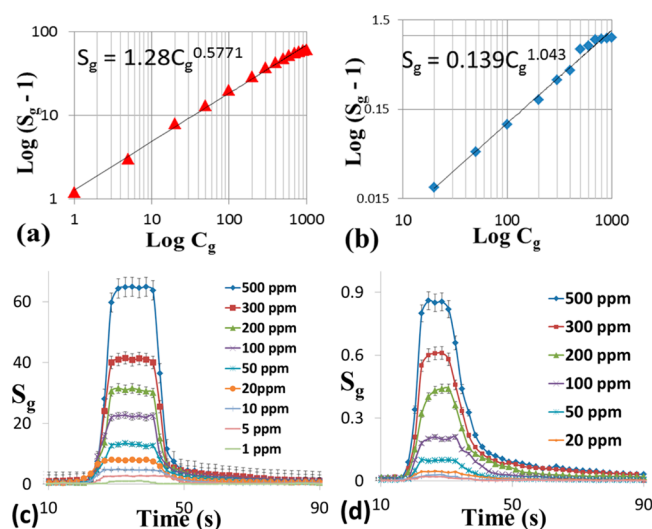
Figure 3. (a,b) Log $(S_g - 1)$ vs log C_g plots of the thermally and UV activated ZND gas sensors, respectively; (c) responses of the thermally activated ZND sensor to ethanol concentration levels from 1 ppm to 500 ppm at 350 °C; (d) responses of the UV activated ZND sensor to ethanol concentration levels from 20 ppm to 500 ppm at 1.6 mW/cm^2.

adsorption sites on the surface of ZnO compared to the number of ethanol molecules, and therefore the surface reaction between ethanol molecules and ZnO surface is the rate-determining step. So, as long as there are sufficient adsorption sites, surface reactions are linearly dependent on the ethanol concentration.

Figure 3c,d shows the responses of the thermally activated ZND sensor to ethanol concentration levels from 1 ppm to 500 ppm and the responses of the UV activated ZND sensor to ethanol concentration levels from 20 ppm to 500 ppm, respectively. The response time and recovery time (defined as the time required for the current to reach 90% of the equilibrium value after injecting the gas and the time necessary for the sensor to return to 10% above the original current value in air after releasing the gas from the test chamber, respectively) for the thermally activated ZND sensor to 100 ppm ethanol are about 11 and 15 s, respectively. With the increase in ethanol concentration, the response time decreases gradually. The response times are calculated to be approximately 8 s for 300 ppm ethanol and 6 s for 500 ppm ethanol. The decrease in response time can be explained by the variation of the saturation time (the time required for complete coverage of the sensor surface by the ethanol molecules) and the mean residence period of ethanol molecules on the ZND surface. At low ethanol concentrations, the time required for the complete reaction of the oxygen species and ethanol molecules is long, leading to a longer response time. As the concentration increases, the reaction time decreases, and the response time decreases accordingly. No obvious change in recovery time can be found in our experiment, which may be due to the high operating temperature under the thermal activation. Moreover, relatively constant base current (I_a) has also been realized among the consecutive tests, which demonstrates the chemical stability of our sensors.

The response time and recovery time for the UV activated ZND sensor exposed to 100 ppm ethanol are 12 and 27 s, respectively. The response time is similar to that of the thermal activation case, but the recovery time is longer, which is attributed to the low operating temperature.

The optimal light intensity was also found to be analyte dependent. Figure 4 shows the plots of light intensity versus
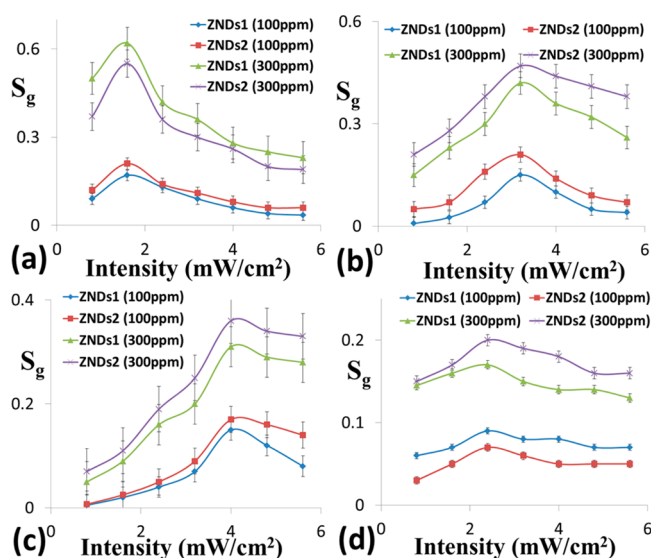
Figure 4. Light intensity vs sensitivity for 100 and 300 ppm of (a) ethanol, (b) acetone, (c) toluene, and (d) isopropanol.

sensitivity for ethanol (Figure 4a), acetone (Figure 4b), toluene (Figure 4c), and isopropanol (Figure 4d). The measured optimum intensity for ethanol was 1.6 mW/cm^2, acetone 3.2 mW/cm^2, toluene 4 mW/cm^2, and isopropanol 2.4 mW/cm^2. From these studies it is proposed that the intensity of the UV irradiation could be used to tune the selectivity of the sensors to specific target volatiles. By sweeping the intensity of the UV from 0.8 to 5.6 mW/cm^2 and looking at the position of the maximum sensitivity value, one can specify the tested gas. These observations are discussed in more detail in the following sections.

In order to eliminate any concentration or material effects, this phenomena was tested using two different sensors and at different concentrations. From Figure 4a−d, it is clear that the concentration of the analyte does not affect the optimum intensity value and reproducibility is high.

Even though the surface-to-volume ratio of the ZND gas sensor (∼10) is similar to that of the ZNW sensor (∼10), our results clearly indicate that the performance characteristics of the gas sensors based on ZNDs are superior to those of the ZNW and ZNS sensors. Based on the morphological and structural analysis of the ZnO nanostructures and considering their different features, it is proposed that the gas sensing ability of ZnO nanostructures is closely related to those of exposed surface structures. In a following section we investigate the relationship between the gas sensing properties and the polarity of the exposed facets of the grown ZnO nanostructures in light of the XPS analysis.

3.3. UV vs Thermal Activation of ZnO Gas Sensors. In order to obtain the best sensing performance, metal oxide sensors are usually operated at high temperatures of 150−400 °C. However, such high temperatures not only lead to high power consumption, but can also ignite flammable and explosive gases. Moreover, the long-term application at high temperatures could result in the growth of the metal oxide grains and consequently lead to long-term drift problems. As an alternative to thermal activation, room temperature UV

activation could be an economical alternative and also allow the development of sensors on portable and flexible substrates.

However, our results indicate that the response level of the UV activated sensors is much lower than the response of the thermally activated devices. In addition, the measurable ethanol concentration levels (1−20 ppm) could not be detected at room temperature. While the two sensing mechanisms under thermal and UV activation for ZnO sensors may be similar, their steady state conditions are qualitatively different.

Stage A in the schematic diagram in Figure 5 shows a ZnO nanostructure under dark conditions at room temperature,
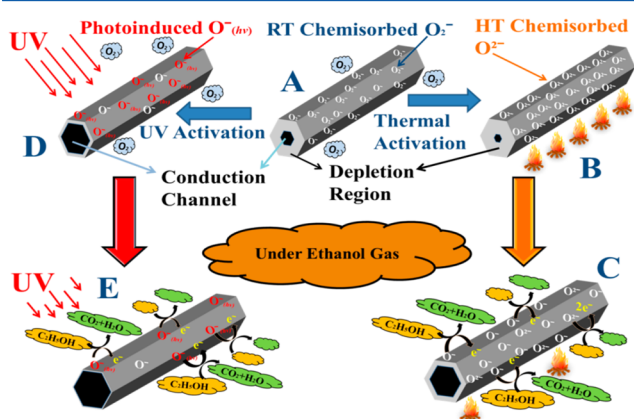
Figure 5. Schematic diagram of the gas sensing mechanism activated thermally and using UV illumination: ZnO nanostructure (A) in air at room temperature, (B) in air at high temperature, (C) under ethanol gas at high temperature, (D) in air under UV illumination, and (E) under ethanol and UV illumination.

where ionized oxygen is chemisorbed onto the surface in its molecular form, O_2^-, as given in eq 3:

$$O_2(gas) + e^- \Leftrightarrow O_2^-(ads)\,(low\ temperature) \quad (3)$$
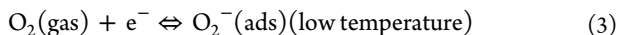
In this form, it is less reactive, which explains the low sensitivity of sensors below 150 °C.[23] At higher temperatures of 150−400 °C, the oxygen ion molecules are dissociated into oxygen ions with singly, O^-, or doubly negative electric charges, O^{2-}, by attracting an electron from the conduction band of the ZnO as shown schematically in stage B of Figure 5 and represented by eqs 4 and 5:

$$1/2 O_2 + e^- \Leftrightarrow O^- ads \quad (4)$$

$$1/2 O_2 + 2e^- \Leftrightarrow O^{2-} ads \quad (5)$$

This significant increase in the steady state resistance due to the depletion of ZnO by the adsorbed oxygen is an indicator of high sensitivity for the thermally activated ZnO gas sensors.[24]
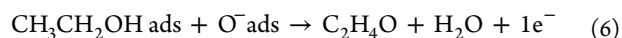
When reducing gases such as ethanol are introduced, the adsorbed oxygen on ZnO nanostructures takes part in the oxidation of ethanol. The oxygen ions on the surface of ZnO react with the ethanol molecules and give up electrons to the conduction band as shown in Stage C of the schematic in Figure 5.

On the contrary, the steady state resistance of a UV activated sensor drops due to continuous UV illumination. This is attributed to the enhanced carrier density in the nanostructure and the reduced surface depletion depth. Once the electron−hole pairs are generated by the UV light, the holes can migrate to the surface and discharge the adsorbed oxygen ions. This
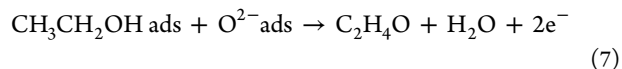
causes the depletion layer depth to decrease, resulting in the desorption of surface oxygen. Over time, the unpaired electrons accumulate until the desorption and adsorption of oxygen reaches an equilibrium state. The amount of adsorbed oxygen decreases compared to dark conditions as shown in Stage D of the schematic in Figure 5. Although initially this looks like a contradiction, the nature of the adsorbed oxygen species is the key factor in the mechanism observed. The presence of excitons under UV irradiation leads to the formation of atomic adsorbed oxygen, O^-, which is substantially more chemically active than O_2^-, and creates favorable conditions for catalytic reactions.[25,26] When reducing gases (such as ethanol in this case) are introduced, the adsorbed oxygen on ZnO nanostructures takes part in the oxidation of ethanol just like in the thermal activation case. The oxygen ions on the surface of ZnO react with the ethanol molecules and give up electrons to the conduction band and increase the carrier concentration in the ZnO nanostructure as shown in Stage E of the schematic in Figure 5.

It is now clear that the two activation mechanisms are similar in many ways; nevertheless, they are different in the nature of the adsorbed oxygen species. As stated previously the oxygen from the atmosphere adsorbs on the surface of the zinc oxide and extracts electrons from its conduction band to form O^- and O^{2-} species on the surface, which leads to the increase in the ZnO sensor resistance. Furthermore, the conversion of the oxygen molecule to O^{2-} would result in the doubling of the surface charge with a thicker depletion layer than that of single ionosorption oxygen (O^-) on the ZnO sensor.[34] This means that the associated carrier concentration of the surface will be lower in the case of O^{2-} formation. This is in agreement with the increased sensitivity of a metal oxide gas sensor at lower carrier concentrations.[24]

From our results, the calculated β value for the thermally activated sensors is close to 0.5 indicating that the oxygen species reacting with ethanol molecules on the surface of the ZnO are O^{2-} ions, while the calculated β value for the UV activated sensors is close to 1 indicating O^- ions. The chemical reaction between ethanol molecules and oxygen ions is shown in eqs 6 and 7 for O^- and O^{2-}, respectively.[27]

$$CH_3CH_2OH\ ads + O^- ads \rightarrow C_2H_4O + H_2O + 1e^- \quad (6)$$

or

$$CH_3CH_2OH\ ads + O^{2-} ads \rightarrow C_2H_4O + H_2O + 2e^- \quad (7)$$

Equations 6 and 7 show that the number of electrons released back to the conduction band of ZnO in the case of O^{2-} ions will be larger than that of the O^- ions. Consequently, the sensitivity of the ZnO sensors with the O^{2-} ions on the surface is far superior to that with the O^- ions. This explains the superior sensitivity of the thermally activated gas sensors over the UV devices.

The changes observed under the different optimal light intensity values for each of the tested gases, although distinct, emphasizes a complicated spectrum of triggers that need verification. However, we believe that different hydrogen bonding values of these gases may play a key role; these are 19.4, 16.4, 7, and 2 kcal/mol for ethanol, isopropanol, acetone, and toluene, respectively. Continuous UV illumination causes the surface of ZnO to be more negatively charged, and this process can be enhanced by increasing the intensity of the UV light. Therefore, increasing the intensity of the UV light results
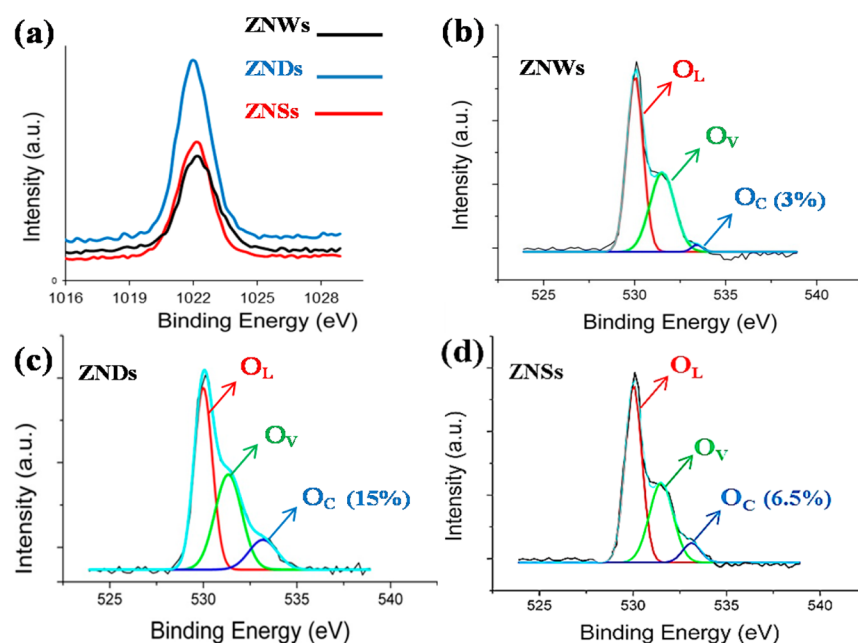
Figure 6. (a) Zn 2p XPS spectra peaks of ZNWs, ZNDs, and ZNSs; (b) O 1s XPS spectra of ZNWs; (c) O 1s XPS spectra of ZNDs; and (d) O 1s XPS spectra of ZNSs. In the figures for (b), (c) and (d), the curves have been fitted with multiple Gaussians, which shows the evolution of the O peaks, which is discussed more fully in the text.

in increased sensitivity. However, the results in Figure 4 show sensitivity decay above a UV intensity threshold value, which varies for different gases. The decay in the sensitivity at higher light intensities can be attributed to higher densities of negative charges on the surface forming stronger hydrogen bonds between the gas molecules and the surface oxygen. These bonds could provide an energy barrier for the gas molecules to escape from the ZnO surface lowering the effective surface area available to sense new analytes. Hence, the onset of decay in sensitivity occurs at relatively lower UV light intensities for gases that can form stronger hydrogen bonds with surface oxygen. Further investigations are underway in order to fully understand and elucidate the mechanism responsible for this selectivity.

3.4. Effect of Exposed Facets of ZnO Nanostructures on Their Gas Sensing Properties. In principle, the gas sensing of a metal oxide semiconductor is a solid–gas interfacial reaction process, which produces an intense change in the resistance of the metal oxide semiconductor. Therefore the chemical adsorption and reaction of target molecules occurring on the surface of metal oxide semiconductors is one of the most crucial factors in its gas sensing behavior.

Recently, significant effort has been made to investigate the influence of the morphology, size, and surface area of metal oxide nanostructures on their gas sensing properties. Recent studies reveal the surface structures and composition to be the essential factors governing the efficiency of gas sensing properties.[28-31] However, the effect of the exposed polar facets on the gas sensing properties of ZnO needs more understanding. In order to obtain useful information about surface structures of as-prepared ZnO nanostructures, XPS analysis was performed. Figure 6a compares the Zn 2p XPS peaks of ZNWs, ZNDs, and ZNSs. The three observed Zn 2p XPS peaks are similar for their position and distribution. Conversely, their corresponding O 1s XPS peaks are different. In fact, all peaks are asymmetric and present a visible shoulder. As shown in Figure 6b–d, each O 1s XPS peak can be decomposed into

three Gaussian components centered at ~530.1 ± 0.15 eV (O_L), 531.5 ± 0.2 eV (O_V), and 532.5 ± 0.15 eV (O_C). According to the literature,[32,33] the O_L component of O 1s spectrum is attributed to O^{2-} ions on wurtzite structure of hexagonal Zn^{2+} ion array, surrounded by Zn atoms with their full complement of nearest-neighbor O^{2-} ions. This means that the quantity of oxygen atoms in a fully oxidized stoichiometric surrounding can be measured by the intensity of this component. The medium binding energy component O_V is associated with O^{2-} ions in oxygen-deficient regions within the matrix of ZnO, while the O_C component is usually attributed to chemisorbed and dissociated oxygen species. Thus, the oxygen-chemisorbed ability of different exposed facets in ZnO crystal can be estimated based on the intensity of O_C component in the O 1s XPS peak. The relative percentages of the O_C component in the three nanostructures are approximately 3% (ZNWs), 15% (ZNDs), and 6.5% (ZNSs), which indicates that the ZNDs may absorb more oxygen species than ZNWs and ZNSs. For example, at ethanol concentration level of 300 ppm, the ratio of the sensitivity of the ZND sensors to that of the ZNS sensors is around 1.85 and the ratio of their corresponding relative percentage of the O_C component is 2.3. Also, the sensitivity ratio of the ZNSs to the ZNWs is around 1.75 and the ratio of their corresponding relative percentage of the O_C component is 2.1. Apparently the gas sensing properties of ZnO are closely related to the chemisorption ability of the crystal surfaces.

The variation in the ability of ZnO nanostructures to absorb oxygen species may also be the reason behind the different optimum operating temperatures (300 °C for the ZNWs and ZNSs and 350 °C for ZNDs). At lower operating temperatures our sensors display high resistance, which then is decreased as the operating temperature increases due to the thermal excitation of electrons. At operating temperatures above 175 °C, the resistance increases as a result of vigorous oxygen adsorptions on the ZnO surface. At this stage the oxygen chemisorption process starts competing with the thermal

excitation of electrons. This competition continues until the complete coverage of ZnO surface with chemisorbed oxygen species, where sensors show the highest sensitivity. Beyond this temperature the sensitivity starts to decrease due to the effect of the dominant thermal excitation of electrons and the saturation of oxygen adsorption on the resistance of the ZnO sensors.[12,34,35] Therefore, it is suggested that the optimum operating temperature of gas sensors based on ZNDs is higher than those of the ZNWs and ZNSs because of their ability to absorb more oxygen species, which is in turn a result of the polarity of the exposed polar facets.

The room-temperature PL spectra of ZnO with different morphologies are shown in Figure 7. In all cases, the spectra
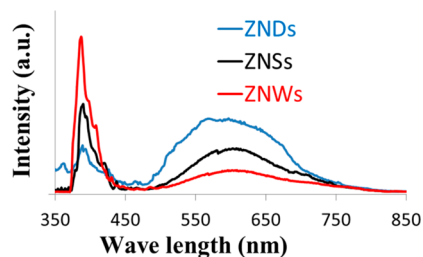
Figure 7. Room temperature PL spectra of the different ZnO morphologies.

show two bands: a luminescence band centered at 386 nm and a broadband in the region of 440−840 nm that has a dominantly strong intensity. The peak centered at 386 nm (3.22 eV) indicates the near-band-edge (3.37 eV) emission and free-exciton peak of ZnO. For the broad luminescence band, it is very clear that the different nanostructures show the following order of intensity: ZNDs > ZNSs > ZNWs. The current PL spectra are generally similar to the ZnO PL spectra reported in the literature.[36,37] The broadband in the visible light region is widely considered to result from ZnO surface defects, in which oxygen vacancies are the most probable source.[36,37] Hence, this PL analysis demonstrates that different ZnO morphologies have various quantities of chemisorbed oxygen, which decrease in turn from ZNDs and ZNSs to ZNWs.

Even though the exposed facets of the ZNWs and ZNSs are similar, their structures are not. We believe that the junction between the arms (NWs) of each ZNS is a key difference. It was reported that these junctions could increase the density of defects which is confirmed by the higher intensity broadband in the region of 440−840 nm of the PL spectra in this work.[38,39] ZNDs are single crystal structures, and therefore the higher intensity of the broadband in the region of 440−840 nm must be due to increased surface defects caused by the exposed polar facets.

Surface properties of metal oxides, including chemical adsorption reactivity,[40,41] such as heterogeneous catalysis, corrosion inhibition, and gas sensing are significantly affected by the density of surface defects. Different theoretical calculations and experimental data have investigated the influence of the intrinsic defects on the ZnO surface chemistry and the effects of chemisorption.[42,43] Additionally, the enhancement in ZnO gas sensing properties caused by the oxygen vacancies has been addressed.[44] A large quantity of oxygen vacancy increases the ability to adsorb oxygen, and in turn enhances the gas sensing properties through a better interaction with tested gases.

The ability to absorb oxygen species (such as O_2^-, O^{2-}, O^-) and target molecules should depend on the atomic structures of the surface. The (0001) facet is terminated with Zn^{2+} ions which are capable of seizing atmospheric oxygen (O_2) through physical/chemical absorption due to unsaturated oxygen coordination. As a result, the (0001) facet has the highest chemisorption ability. Most of the exposed surfaces of ZNDs are the Zn-terminated (0001) facets, and accordingly its performance as a gas sensor is significantly enhanced. On the other hand, the dominating exposed surfaces of ZNWs and ZNSs are the nonpolar $\{10\bar{1}0\}$ planes with equivalent Zn atoms and O atoms in the same plane, so their gas sensing properties are not as good as the (0001) plane. Based on the discussion above, it can be concluded in principle that the gas sensing ability of the ZnO crystal facets is (0001) > $\{10\bar{1}0\}$, which is reflected in our experimental results where the sensitivity of the ZND gas sensors, with more exposed polar facets, is superior to that of the ZNW and ZNS sensors.

4. CONCLUSION

In conclusion, we have synthesized ZNWs, ZNDs, and ZNSs, with different fractions of exposed polar facets, by facile hydrothermal processes. The relationship between surface polarity and gas sensing properties has been studied. On the basis of related XPS and structural analysis, it is evident that the gas sensing properties of the ZnO nanostructures with different morphologies depend on the chemsorption ability of the exposed facets. The Zn terminated surfaces have the highest chemsorption ability and therefore have the highest gas sensitivity.

Furthermore, we investigated the performance of ZnO gas sensors under thermal and UV activation. The two activation mechanisms were compared and a consistent model for room temperature UV activated gas sensor was demonstrated. We also demonstrated that by adjusting the UV light intensity the selectivity of the UV activated gas sensor can be enhanced.

■ AUTHOR INFORMATION

Corresponding Author
*E-mail: s.silva@surrey.ac.uk.

Notes
The authors declare no competing financial interest.

■ REFERENCES

(1) Greene, L. E.; Yuhas, B. D.; Law, M.; Zitoun, D.; Yang, P. Solution-Grown Zinc Oxide Nanowires. *Inorg. Chem.* **2006**, *45*, 7535−7543.

(2) Wang, Z. L. ZnO nanowire and nanobelt platform for nanotechnology. *Mater. Sci. Eng.* **2009**, *64*, 33−71.

(3) Ashfold, M. N. R.; Claeyssens, F.; Fuge, G. M.; Henley, S. J. Pulsed laser ablation and deposition of thin films. *Chem. Soc. Rev.* **2004**, *33*, 23−31.

(4) Jayawardena, K. D. G. I.; Opoku, C.; Fryar, J.; Silva, S. R. P.; Henley, S. J. Excimer laser accelerated hydrothermal synthesis of ZnO

nanocrystals & their electrical properties. *Appl. Surf. Sci.* **2010**, *257*, 5274−5277.

(5) Kolmakov, A.; Klenov, D. O.; Lilach, Y.; Stemmer, S.; Moskovits, M. Enhanced Gas Sensing by Individual SnO2 Nanowires and Nanobelts Functionalized with Pd Catalyst Particles. *Nano Lett.* **2005**, *5*, 667−673.

(6) Sysoev, V. V.; Goschnick, J.; Schneider, T.; Strelcov, E.; Kolmakov, A. A Gradient Microarray Electronic Nose Based on Percolating SnO2 Nanowire Sensing Elements. *Nano Lett.* **2007**, *7*, 3182−3188.

(7) Ra, H. W.; Khan, R.; Kim, J. T.; Kang, B. R.; Im, Y. H. The effect of grain boundaries inside the individual ZnO nanowires in gas sensing. *Nanotechnology* **2010**, *21*, 085502−085507.

(8) Barsan, N.; Weimar, U. Conduction Model of Metal Oxide Gas Sensors. *J. Electroceram.* **2001**, *7*, 143−167.

(9) Rider, K. B.; Hwang, K. S.; Salmeron, M.; Somorjai, G. A. High Pressure (1 Torr) Scanning Tunneling Microscopy (STM) Study of the Coadsorption and Exchange of CO and NO on the Rh(111) Crystal Face. *J. Am. Chem. Soc.* **2002**, *124*, 5588−5593.

(10) Tillekaratne, A.; Siap, D.; Trenary, M. Adsorption and Dehydrogenation of ortho-Carborane on the Pt(111) Surface. *J. Phys. Chem. C* **2008**, *112*, 8682−8689.

(11) Jin, J. M.; Lin, W. F.; Christensen, P. A. The effects of the specific adsorption of anion on the reactivity of the Ru(0001) surface towards CO adsorption and oxidation: in-situ FTIRS studies. *Phys. Chem. Chem. Phys.* **2008**, *10*, 3774−3783.

(12) Tian, S.; Yang, F.; Zeng, D.; Xie, D. Solution-Processed Gas Sensors Based on ZnO Nanorods Array with an Exposed (0001) Facet for Enhanced Gas-Sensing Properties. *J. Phys. Chem. C* **2012**, *116*, 10586−10591.

(13) Fan, S. W.; Srivastava, A. K.; Dravid, V. P. UV-activated room-temperature gas sensing mechanism of polycrystalline ZnO. *Appl. Phys. Lett.* **2009**, *95*, 142106:1−142106:3.

(14) Luo, L.; Sosnowchik, B. D.; Lin, L. Local vapor transport synthesis of zinc oxide nanowires for ultraviolet-enhanced gas sensing. *Nanotechnology* **2010**, *21*, 495502−495508.

(15) J. Saura, J. Gas-sensing properties of SnO$_2$ pyrolytic films subjected to UV radiation. *Sens. Actuators, B* **1994**, *17*, 211−214.

(16) Mishra, S.; Ghanshyam, C.; Ram, N.; Bajpai, R. P.; Bedi, R. K. Detection mechanism of metal oxide gas sensor under UV radiation. *Sens. Actuators, B* **2004**, *97*, 387−390.

(17) Wang, Z. L. Novel nanostructures of ZnO for nanoscale photonics, optoelectronics, piezoelectricity, and sensing. *Appl. Phys. A: Mater. Sci. Process* **2007**, *88*, 7−15.

(18) Zhou, X.; Xie, Z. X.; Jiang, Z. Y.; Kuang, Q.; Zhang, S. H.; Xu, T.; Huang, R. B.; Zheng, L. S. Formation of ZnO hexagonal micro-pyramids: A successful control of the exposed polar surfaces with the assistance of anionic liquid. *Chem. Commun.* **2005**, *44*, 5572−5574.

(19) Li, G. R.; Hu, T.; Pan, G. L.; Yan, T. Y.; Gao, X. P.; Zhu, H. Y. Morphology-function relationship of ZnO: Polar planes, oxygen vacancies, and activity. *J. Phys. Chem. C* **2008**, *112*, 11859−11864.

(20) Xu, S.; Wang, Z. L. One-dimensional ZnO nanostructures: Solution growth and functional properties. *Nano Res.* **2011**, *4* (11), 1013−1098.

(21) Herrán, J.; Fernández-González, O.; Castro-Hurtado, I.; Romero, T.; Mandayo, G. G.; Castaño, E. Photoactivated solid-state gas sensor for CO$_2$ detection at room temperature. *Sens. Actuators, B* **2010**, *149*, 368−372.

(22) Feng, P.; Xue, X. Y.; Liu, Y. G.; Wang, T. H. Highly sensitive ethanol sensors based on {100}-bounded In$_2$O$_3$ nanocrystals due to face contact. *Appl. Phys. Lett.* **2006**, *89*, 243514(1)−(3).

(23) Capone, S.; Forleo, A.; Francioso, L.; Rella, R.; Siciliano, P.; Spadavecchia, J.; Presicce, D. S.; Taurino, A. M. Solid state gas sensors state of the art and future activities. *J. Optoelectron. Adv. Mater.* **2003**, *5*, 1335−1348.

(24) Al-Hardan, N.; Abdullah, M. J.; Abdul Aziz, A. The gas response enhancement from ZnO film for H 2 gas detection. *Appl. Surf. Sci.* **2009**, *255*, 7794−7797.

(25) Barry, T.; Stone, F. The Reactions of Oxygen at Dark and Irradiated Zinc Oxide Surface. *Proc. R. Soc. London, Ser. A* **1960**, *255*, 124−144.

(26) Fan, S.; Srivastava, A. K.; Dravid, P. V. UV-activated room-temperature gas sensing mechanism of polycrystalline ZnO. *Appl. Phys. Lett.* **2009**, *95*, 142106(1)−(3).

(27) Kwak, G.; Yong, K. Adsorption and Reaction of Ethanol on ZnO Nanowires. *J. Phys. Chem. C* **2008**, *112*, 3036−3041.

(28) Xiong, S. L.; B. Xi, J.; Wang, C. M.; Xu, D. H.; Feng, X. M.; Zhu, Z. C.; Qian, Y. T. Tunable Synthesis of Various Wurtzite ZnS Architectural Structures and Their Photocatalytic Properties. *Adv. Funct. Mater.* **2007**, *17*, 2728−2738.

(29) Rout, C. S.; Krishna, S. H.; Vivekchand, S. R. C.; Govindaraj, A.; Rao, C. N. R. Hydrogen and ethanol sensors based on ZnO nanorods, nanowires and nanotubes. *Chem. Phy. Lett.* **2006**, *418*, 586−590.

(30) Xu, J. Q.; Pan, Q. Y.; Shun, Y. A.; Tian, Z. Z. Grain size control and gas sensing properties of ZnO gas sensor. *Sens. Actuators, B* **2000**, *66*, 277−279.

(31) Németh, Á.; Horváth, E.; Lábadi, Z.; Fedák, L.; Bársony, I. Single step deposition of different morphology ZnO gas sensing films. *Sens. Actuators, B* **2007**, *127*, 157−160.

(32) Hsieh, P. T.; Chen, Y. C.; Kao, K. S.; Wang, C. M. Luminescence mechanism of ZnO thin film investigated by XPS measurement. *Appl. Phys. A: Mater. Sci. Process* **2008**, *90*, 317−321.

(33) Chen, M.; Wang, X.; Yu, Y. H.; Pei, Z. L.; Bai, X. D.; Sun, C.; Huang, R. F.; Wen, L. S. X-ray photoelectron spectroscopy and auger electron spectroscopy studies of Al-doped ZnO films. *Appl. Surf. Sci.* **2000**, *158*, 134.

(34) Sahay, P. P.; Nath, R. K. Al-doped zinc oxide thin films for liquid petroleum gas (LPG) sensors. *Sens. Actuators, B* **2008**, *133*, 222−227.

(35) Kwon, C. H.; Hong, H. K.; Yun, D. H.; Lee, K.; Kim, S. T.; Roh, Y. H.; Lee, B. Thick-film Zinc-oxide Gas Sensor for the Control of Lean Air-to-fuel Ratio in Domestic Combustion Systems. *Sens. Actuators, B* **1995**, *24/25*, 610−613.

(36) Djurisic, A. B.; Choy, W. C. H.; Roy, V. A. L.; Leung, Y. H.; Kwong, C. Y.; Cheah, K. W.; Rao, T. K. G.; Chan, W. K.; Lui, H. F.; Surya, C. Photoluminescence and Electron Paramagnetic Resonance of ZnO Tetrapod Structures. *Adv. Funct. Mater.* **2004**, *14*, 856−864.

(37) Wu, X. L.; Siu, G. G.; Fu, C. L.; Ong, H. C. Photoluminescence and cathodoluminescence studies of stoichiometric and oxygen-deficient ZnO films. *Appl. Phys. Lett.* **2001**, *78*, 2285−2288.

(38) Zhang, D. H.; Liu, Z. Q.; Li, C.; Tang, T.; Liu, X. L.; Han, S.; Lei, B.; Zhou, C. W. Detection of NO$_2$ down to ppb Levels Using Individual and Multiple In$_2$O$_3$ Nanowire Devices. *Nano Lett.* **2004**, *4*, 1919−1924.

(39) Zhang, Y.; Xu, J.; Xiang, Q.; Li, H.; Pan, Q.; Xu, P. Brush-Like Hierarchical ZnO Nanostructures: Synthesis, Photoluminescence and Gas Sensor Properties. *J. Phys. Chem. C* **2009**, *113*, 3430−3435.

(40) Gutierrez-Sosa, G. A.; Baraldi, A.; Larciprete, R.; Lizzit, S. Impact of defects on the surface chemistry of ZnO(0001 macro)-O. *J. Am. Chem. Soc.* **2002**, *124*, 7117−1722.

(41) Lindsay, R.; Michelangeli, E.; Daniels, B. G.; Ashworth, T. V.; Limb, A. J.; Thornton Geistlinger, H. The influence of chemisorption on the defect equilibrium of metal oxide thin films. *J. Appl. Phys.* **1996**, *80*, 1370−1380.

(42) Göpel, W. Reactions of oxygen with ZnO−10$\overline{1}$0-surfaces. *J. Vac. Sci. Technol.* **1978**, *15*, 1298−1311.

(43) An, W.; Wu, X. Q.; Zeng, X. C. Adsorption of O$_2$, H$_2$, CO, NH$_3$, and NO$_2$ on ZnO Nanotube: A Density Functional Theory Study. *J. Phys. Chem. C* **2008**, *112*, 5747−5755.

(44) Liao, L.; Lu, H. B.; Li, J. C.; He, H.; Wang, D. F.; Fu, D. J.; Liu, C.; Zhang, W. F. Size Dependence of Gas Sensitivity of ZnO Nanorods. *J. Phys. Chem. C* **2007**, *111*, 1900−1903.